MOSEL Survey: Tracking the Growth of Massive Galaxies at $2 < z < 4$ Using Kinematics and the IllustrisTNG Simulation

Anshu Gupta[1,2] ⓘ, Kim-Vy Tran[1,2,3] ⓘ, Jonathan Cohn[3] ⓘ, Leo Y. Alcorn[3,4] ⓘ, Tiantian Yuan[2,5] ⓘ, Vicente Rodriguez-Gomez[6],
Anishya Harshan[1] ⓘ, Ben Forrest[7] ⓘ, Lisa J. Kewley[2,8] ⓘ, Karl Glazebrook[5] ⓘ, Caroline M. Straatman[9] ⓘ, Glenn G. Kacprzak[2,5],
Themiya Nanayakkara[10] ⓘ, Ivo Labbé[5] ⓘ, Casey Papovich[3,11] ⓘ, and Michael Cowley[12,13] ⓘ
[1] School of Physics, University of New South Wales, Sydney, NSW 2052, Australia; anshu.gupta@unsw.edu.au
[2] ARC Centre of Excellence for All Sky Astrophysics in 3 Dimensions (ASTRO 3D), Australia
[3] George P. and Cynthia Woods Mitchell Institute for Fundamental Physics and Astronomy, Texas A&M University, College Station, TX 77843-4242, USA
[4] Department of Physics and Astronomy, York University, 4700 Keele Street, Toronto, Ontario, MJ3 1P3, Canada
[5] Swinburne University of Technology, Hawthorn, VIC 3122, Australia
[6] Instituto de Radioastronomía y Astrofísica, Universidad Nacional Autónoma de México, A.P. 72-3, 58089 Morelia, Mexico
[7] Department of Physics & Astronomy, University of California, Riverside, 900 University Avenue, Riverside, CA 92521, USA
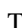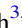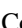[8] Research School of Astronomy and Astrophysics, The Australian National University, Cotter Road, Weston Creek, ACT 2611, Australia
[9] Sterrenkundig Observatorium, Universiteit Gent, Krijgslaan 281 S9, B-9000 Gent, Belgium
[10] Leiden Observatory, Leiden University, P.O. Box 9513, NL 2300 RA Leiden, The Netherlands
[11] Department of Physics and Astronomy, Texas A&M University, College Station, TX 77843-4242, USA
[12] Centre for Astrophysics, University of Southern Queensland, West Street, Toowoomba, QLD 4350, Australia
[13] School of Chemistry, Physics and Mechanical Engineering, Queensland University of Technology, Brisbane, QLD 4001, Australia

Abstract

We use K-band spectroscopic data from the Multi-Object Spectroscopic Emission Line survey to analyze the kinematic properties of galaxies at $z > 3$. Our sample consists of 34 galaxies at $3.0 < z_{\rm spec} < 3.8$ between $9.0 < \log(M_*/M_\odot) < 11.0$. We find that galaxies with $\log(M_*/M_\odot) > 10.2$ at $z > 3$ have 56 ± 21 km s^{-1} lower integrated velocity dispersion compared to galaxies at $z \simeq 2$ of similar stellar mass. Massive galaxies at $z > 3$ have either a flat or declining star formation history (SFH), whereas similar stellar mass galaxies at $z \sim 2.0$ exhibit a slight peak in the past 500 Myr. Comparing with the IllustrisTNG cosmological simulation, we find that (i) the dynamical mass of massive galaxies in simulations ($\log(M_*/M_\odot) > 10.0$) increases by ~ 0.1 dex at a fixed stellar mass between $z = 2.0$–3.0, and (ii) dynamical mass growth is coupled with a rapid rise in the ex situ stellar mass fraction (stars accreted from other galaxies) for massive galaxies at $z < 3.5$. We speculate that the rising contribution of ex situ stellar mass to the total stellar mass growth of massive galaxies is driving the higher integrated velocity dispersion and rising SFHs of massive galaxies at $z \sim 2.0$ compared to galaxies of similar stellar masses at $z > 3$.

Unified Astronomy Thesaurus concepts: High-redshift galaxies (734); Galaxy evolution (594); Galaxy kinematics (602); Spectroscopy (1558)

1. Introduction

The kinematic properties of star-forming galaxies (SFGs) are intimately related to their mass assembly histories, including both the baryonic (gas and stars) and dark matter assembly. Various spectroscopic surveys have extended our understanding of the kinematic evolution of galaxies beyond the local universe (Epinat et al. 2012; Sobral et al. 2013; Wisnioski et al. 2015; Alcorn et al. 2016; Stott et al. 2016; Straatman et al. 2017; Girard et al. 2018). The kinematic observations of galaxies at $z > 1$ reveal an increasing baryonic fraction of galaxies with redshift, suggesting an ongoing assembly of dark matter (Gnerucci et al. 2011; Lang et al. 2017; Genzel et al. 2017; Straatman et al. 2017; Price et al. 2019).

The mass assembly history of massive SFGs is different from the assembly history of low mass galaxies. Massive galaxies ($\log(M_*/M_\odot) \approx 11$ at $z = 0$) acquire almost 40% of their mass via ex situ processes such as mergers below $z < 2$, whereas low mass galaxies mostly grow by in situ star formation and gas accretion (Nipoti et al. 2009; Lee & Yi 2013; Rodriguez-Gomez et al. 2016). Rodriguez-Gomez et al. (2016), using Illustris simulations, find that for the most massive galaxies ($\log(M_*/M_\odot) \approx 12$) at $z = 0$, the stellar mass assembly history transitions from in situ to ex situ growth at

around $z \sim 1.0$, whereas the stellar mass assembly of low mass galaxies ($\log(M_*/M_\odot) \approx 10$ at $z = 0$) is dominated by the in situ star formation at all epochs.

Observational signatures of transition in the mass assembly histories of massive galaxies are limited. SFGs with compact, dense cores at $z \sim 2.0$ are speculated to be progenitors of present-day early-type galaxies that transform into elliptical galaxies by the addition of ex situ stellar mass from dry mergers (Barro et al. 2013, 2014; Nelson et al. 2014; Wellons et al. 2016). Nelson et al. (2014) and Barro et al. (2014) find compact SFGs at $z \sim 2.0$ with $\log(M_*/M_\odot) \sim 10.8$–11.0 that have integrated velocity dispersions nearly equal to the stellar velocity dispersions of massive quiescent galaxies at $z \sim 2.0$.

In this paper, we show that kinematic properties of galaxies at $z > 3$ are consistent with the transitory phase (in situ to ex situ growth) in the assembly history of massive galaxies between $z = 2$–3. Current investigations into the kinematics of galaxies at $z > 3.0$ are limited by the small number of galaxies, especially with $\log(M_*/M_\odot) > 10.0$ (Law et al. 2009; Gnerucci et al. 2011; Livermore et al. 2015; Turner et al. 2017; Girard et al. 2018; Price et al. 2019). We use the K-band spectroscopic data from the Multi-Object Spectroscopic Emission Lines (MOSEL) survey (Tran et al. 2020). We derive star

formation histories (SFHs) of our MOSEL targets using the spectral energy distribution (SED) fitting code PROSPECTOR (Leja et al. 2017) and compare our results with the dynamical mass estimates from the IllustrisTNG simulations (Nelson et al. 2018; Pillepich et al. 2018).

This paper is organized as follows. We discuss our methodology and observations in Section 2. In Section 2.1, we describe the sample selection, observations, and data reduction for the MOSEL survey. Section 3 presents our results from the observations. In Section 4, we compare our results with IllustrisTNG simulations. Finally, in Section 5 we discuss the main implications of our results and summarize them in Section 6.

For this work, we assume a flat ΛCDM cosmology with $\Omega_M = 0.3$, $\Omega_\Lambda = 0.7$, and $h = 0.7$. The only exception is the PROSPECTOR software, where a WMAP9 cosmology (Hinshaw et al. 2013) cosmology is used.

2. Observations

2.1. MOSEL Survey

Our sample is drawn from the MOSEL survey, which is a spectroscopic follow-up of the $z \sim 3$ galaxies selected from the FourStar Galaxy Evolution survey (ZFOURGE; Straatman et al. 2016). The ZFOURGE survey uses the medium J-band filters J_1, J_2, and J_3, and medium H-band filters H_s and H_l, and deep K_s filters, to target specific spectral features for galaxies at $2.5 < z < 4$. Thus, the ZFOURGE survey reaches a photometric redshift accuracy of $\sigma_z = 0.016$ in the redshift range $2.5 < z < 4.0$ (Straatman et al. 2016). The ZFIRE survey confirms the precision of the photometric redshift measurements of the ZFOURGE survey to $\sigma_z \sim 2\%$ (Nanayakkara et al. 2016).

We refer to Tran et al. (2020) for a detailed description of the MOSEL survey design. In summary, the MOSEL survey acquires near-infrared spectra of the emission line galaxies between $3.0 < z < 3.8$ to understand their contribution to the SFH of the universe. The MOSEL survey uses the emission line strength defined as [O III]+Hβ equivalent widths (EWs) from the composite SED fitting by Forrest et al. (2018) to identify emission line galaxies. Based on the strength of the [O III]+Hβ EW, the MOSEL survey classifies emission line galaxies at $2.5 < z < 4$ as follows: extreme emission line galaxies with [O III]+Hβ EW > 800 Å, strong emission line galaxies with [O III]+Hβ EW 230–800 Å, and star-forming galaxies with [O III]+Hβ EW 0–230 Å.

Throughout this paper, we use stellar masses derived in the ZFOURGE survey using the SED fitting code FAST (Kriek et al. 2009) for both the MOSEL and ZFIRE galaxy samples.

2.2. Keck/MOSFIRE Observations

Keck/MOSFIRE (McLean et al. 2012) observations were taken on 2017 February 12 and 13 (project code Z245, PI Kewley). A total of five masks were observed in the COSMOS field and one mask in the CDFS field in the K-band filter covering a wavelength of 1.93–2.38 μm. The spectral dispersion is 2.17 Å/pixel. The seeing was $\sim$0″.7.

A total of 95 galaxies were targeted between $0.9 < z < 4.8$, with highest priority given to the emission line galaxies with [O III]+Hβ EW > 230 Å (38 galaxies) between $2.5 < z < 4.0$. Possible active galactic nuclei (AGNs) contaminants were removed using the Cowley et al. (2016) catalog that uses X-ray,

radio, and infrared imaging to identify AGNs in the ZFOURGE survey. The data was reduced using the MOSFIRE data reduction pipeline[14] and flux calibration was performed using the ZFIRE data reduction pipeline (Tran et al. 2015; Nanayakkara et al. 2016).

We spectroscopically confirm 48 galaxies between $2.9 < z < 3.8$, of which 11 are extreme emission line galaxies, 13 are strong emission line galaxies, and 24 are star-forming galaxies (Tran et al. 2020). We also add data for $z > 3.0$ galaxies observed in the ZFIRE survey. The median redshift of our sample is $z_{\rm spec} = 3.4$. We reach a final sample of 34 galaxies after selecting galaxies with signal-to-noise ratio (S/N) greater than three (see Section 2.3) and GALFIT residuals <20% (see Section 2.4).

2.3. Emission Line Flux and Kinematic Measurements

We use the flux calibrated and telluric corrected 2D slit spectra from the MOSEL survey and $z > 3$ galaxies from the ZFIRE survey (Tran et al. 2015; Nanayakkara et al. 2016) to extract emission line fluxes. We collapse the 2D slit spectra along the wavelength axis to generate the spatial profile and fit a Gaussian. To generate the 1D spectra, we sum the 2D slit spectra within two times the full width at half maximum from the centroid of the spatial profile. To generate an error 1D spectrum, we sum the noise 2D slit spectrum in quadrature within the same aperture as the 1D flux spectrum.

We initially manually identified the line centroid to provide an initial galaxy redshift. This was possible given the high S/N of the emission lines. We then deredshifted the spectra and computed the final galaxy redshifts along with the emission line fluxes after performing a Gaussian fit to emission lines. We simultaneously fit the [O III] λ5007, [O III] λ4959, and Hβ λ4861 emission lines with three Gaussians and five free parameters: redshift, flux-[O III], flux-Hβ, width, and continuum level. We fix the [O III] λ4959 flux to be [O III] λ5007/ 3. For galaxies where Hβ S/N is <3, we refit the 1D spectrum including only [O III] λ5007 and [O III] λ4959 emission lines with two Gaussians and four free parameters: redshift, flux-[O III], width, and continuum level.

The instrumental broadening is measured from the width of the skylines in the K-band in the error spectrum near 5007 Å in wavelength units and is 0.55 Å (32 km s^{-1}). While fitting emission lines, we subtract the instrumental broadening in quadrature from the Gaussian line width. For galaxies where only a single emission line was detected, we assume that emission line identification is correct if the difference between ZFOURGE photometric redshifts and the spectroscopic redshift is less than 2% (Tran et al. 2015; Nanayakkara et al. 2016).

Even in the best seeing conditions (0″.5) galaxies at $z \sim 3$ cannot be resolved with MOSFIRE. We resort to using the integrated velocity dispersion ($\sigma_{\rm int}$) measured using the integrated line width to estimate the kinematic properties of galaxies. We determine the integrated velocity dispersion using the best-fit line width to the highest S/N line [O III] λ5007.

Figure 1 shows two randomly selected sample spectra. For each galaxy, we create 1000 realizations of the flux spectrum by perturbing the flux spectrum according to the noise spectrum (shown as a gray shaded region in Figure 1). For each realization, we perform the previously described fitting routine to remeasure the emission line fluxes and the
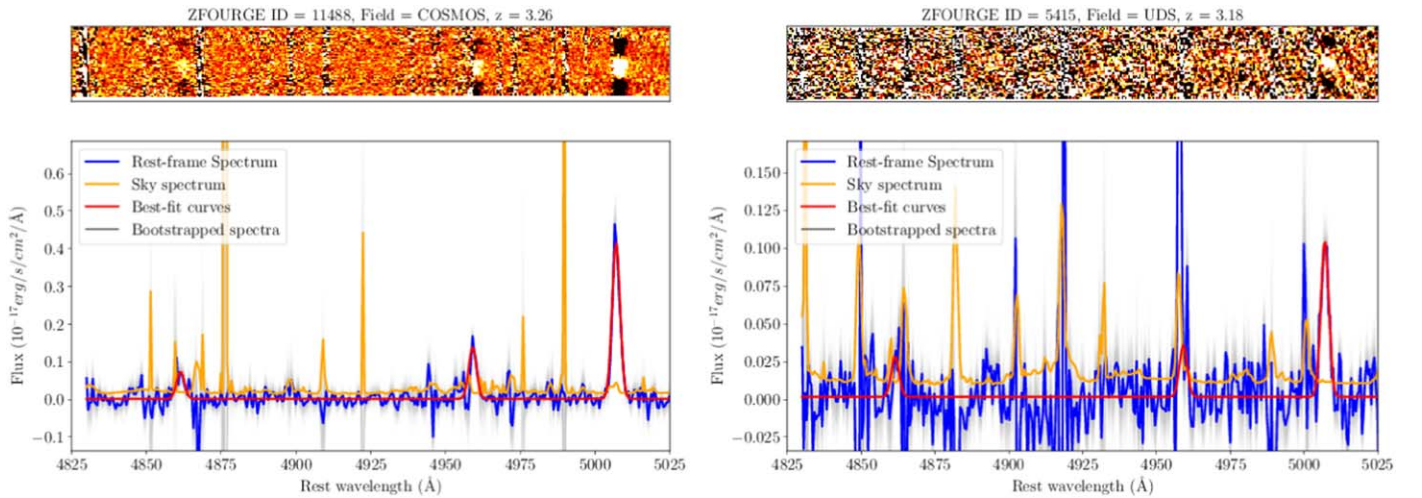
---

[14] http://keck-datareductionpipelines.github.io/MosfireDRP

Figure 1. Sample spectra for two MOSEL galaxies from MOSFIRE observations. The blue curves are the observed 1D spectra in the rest frame, orange lines are the corresponding noise spectra, and the gray shaded region is the bootstrapped iterations. The red curves correspond to the best-fit curves to the [O III] $\lambda\lambda5007,4959$ and Hβ $\lambda4861$ emission lines. The images in the top panels show the corresponding 2D spectrum for each galaxy. We provide MOSFIRE spectra of all massive MOSEL galaxies in Figure 10.
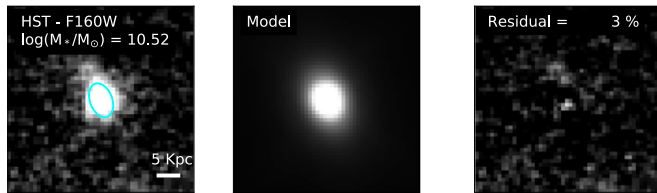

Figure 2. *HST*-F160W image (left) of a sample galaxy from the MOSEL survey. The middle and the right panels show the best-fit spatial profiles and residuals, respectively, from GALFIT. The cyan ellipse in the left panel indicates the best-fit ellipse along the semimajor axis with a radius equal to the twice the effective radius. The legend in the right panel indicates the percentage residuals summed in quadrature within twice the effective radius. For velocity dispersion and dynamical mass analysis, we select galaxies with the total percentage residuals <20%. We provide GALFIT models for all massive MOSEL galaxies in Figure 11.

instrumental dispersion corrected integrated velocity dispersion (σ_{int}). The standard deviation from the bootstrapped versions represents the noise in the line flux and line width measurements. All our results have been quoted with at least [O III] $\lambda5007$ detections at a S/N greater than 3.

2.4. HST *Imaging*

To measure effective radii of galaxies, we use Cosmic Assembly Near-Infrared Deep Extragalactic Survey (CAN-DELS; Grogin et al. 2011; Koekemoer et al. 2011) imaging. We use the composite point-spread function images for the *HST* filters from the 3D-*HST* survey (Brammer et al. 2012). We measure the effective radius (R_e) using the GALFIT software (Peng et al. 2010) and *HST*-F160W images.

We fit a single Sérsic profile to galaxies, with initial parameters for the disk size, axis ratio, and position angles taken from van der Wel et al. (2014) and visual inspection. Only ~20% of our MOSEL targets had effective radius measurements in the original van der Wel et al. (2014) catalog. We ran GALFIT on our galaxies in an automated fashion and visually inspected the residual images to determine the goodness of fit. We use the following constraints during the automated Sérsic profile fitting: centroid $\Delta x = \pm3$ pixels, $\Delta y = \pm3$ pixels,
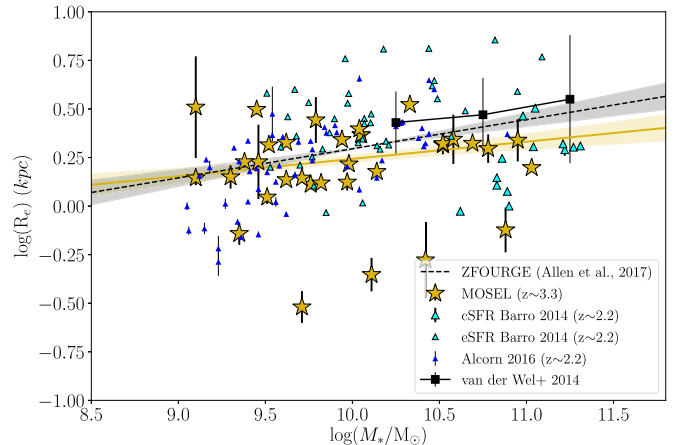

Figure 3. The stellar mass vs. effective F160W radii (R_e) relation for MOSEL galaxies (gold stars), where R_e was derived using GALFIT. The gold shaded region is the best-fit linear relation between the $\log(R_e)$ and stellar mass. The black dashed line is stellar mass–size relation for galaxies between $z = 3$–4 from the ZFOURGE survey by Allen et al. (2016). The black squares show the median and 16th and 84th percentile in the size of late-type galaxies at $z = 2.75$ from van der Wel et al. (2014). We compare our measurements with various star-forming galaxy samples at $z \sim 2$, (Barro et al. 2014; Alcorn et al. 2016).

Sérsic index = 0.7–4, $\Delta R_e = \pm3$ pixels, and Δposition angle = $\pm10°$. Galaxies with poor fits were refitted by varying the initial parameters until a good fit was obtained or the galaxy was deemed to have too low S/N for a reasonable fit.

We use the GALFIT best-fit parameters to determine the sizes, axis ratios, and position angles of galactic disks on the sky. We measure the residual fraction for each galaxy by summing the residual image in quadrature within the galactic disk and dividing by the total flux within the same region. Throughout this paper, we use galaxies that have total residual flux after surface brightness fitting less than 20%.

Figure 2 shows an example of the surface brightness profile fit for a randomly selected galaxy. Figure 3 shows the derived relation between stellar mass and the semimajor axis radii from GALFIT as effective radii for our MOSEL targets. We find that

our effective radii measurements are within 1σ error compared to effective radii measurements in the van der Wel et al. (2014) catalog. We note that our best-fit stellar mass–size relation for the MOSEL sample is slightly below the 1σ stellar mass–size relation derived by Allen et al. (2016) for $z = 3$–4 galaxies from the ZFOURGE survey. However, there is a lot of scatter in the mass–size relation at $z > 3$ at the massive end due to small number statistics.

2.5. Star Formation Histories from PROSPECTOR

PROSPECTOR uses a Flexible Stellar Population Synthesis package (Conroy et al. 2009; Conroy & Gunn 2010) where the contribution of dust attenuation, nebular emission, and re-radiation was modeled Byler et al. (2017). We use the parameters used by Cohn et al. (2018) to the SFHs, i.e., using a Chabrier (2003) initial mass function (IMF) with MESA Isochrones & Stellar Tracks (MIST; Paxton et al. 2011, 2013, 2015; Choi et al. 2016; Dotter 2016), and a Calzetti et al. (1994) dust attenuation model with a WMAP9 cosmology (Hinshaw et al. 2013). We fit nine free parameters: stellar mass, stellar and gas-phase metallicity, dust attenuation, and five independent nonparametric SFH bins.

PROSPECTOR fits nonparametric SFHs by fitting the fraction of stellar mass formed in a particular time bin, after fitting for the total stellar mass (Leja et al. 2019a). To isolate the emission from young and old stars, we use the following time bins: 0–50 Myr, 50–100 Myr, 100–500 Myr, 0.5–1.0 Gyr, and two evenly spaced time bins from 1 Gyr to the age of the universe at the redshift of a given galaxy. PROSPECTOR fits for six SFH bins but the additional constraint on fractional stellar mass to be one results in only five independent SFH bins. We use a uniform prior on SFH corresponding to a constant star formation rate.

3. Kinematics and SFHs of Galaxies at $z > 3$

3.1. Kinematics of MOSEL Galaxies

The integrated velocity dispersion represents a combination of the rotation and the intrinsic velocity dispersion of galaxies (Glazebrook 2013; Barro et al. 2014). We use the integrated velocity dispersion from the [O III] emission line to analyze the evolution of the gravitational potential and the intersic velocity dispersion of $z > 3$ galaxies from our MOSEL survey. Resolving kinematics for $z \sim 3$ galaxies with MOSFIRE is not possible because of the small disk size of $z > 3$ galaxies and seeing-limited conditions.

Figure 4 shows $\log(\sigma_{int})$ as a function of the stellar mass for MOSEL galaxies. We select galaxies with $S/N > 3$ on [O III] $\lambda5007$ (Figure 1) and small GALFIT ($<20\%$) residuals (Figure 2). The limited spectral and spatial resolution of MOSFIRE at $z \sim 3.0$ prevents full kinematic decomposition of galaxies similar to Straatman et al. (2017), restricting us to $\log(\sigma_{int})$ measurements.

3.1.1. Selecting the Stellar Mass Cut-off

We use k-Means, a Python-based unsupervised learning clustering algorithm from the scikit-learn (Pedregosa et al. 2012) library, to identify two subgroups of MOSEL galaxies on the $\log(\sigma_{int})$ versus stellar mass plane, separated at a stellar mass of $\log(M_*/M_\odot) = 10.2$. The two identified subgroups have the locations g1: $\log(M_*/M_\odot) = 9.7$, $\log(\sigma_{int}) = 1.91$,; and g2: $\log(M_*/M_\odot) = 10.7$, $\log(\sigma_{int}) = 2.05$. The stellar mass

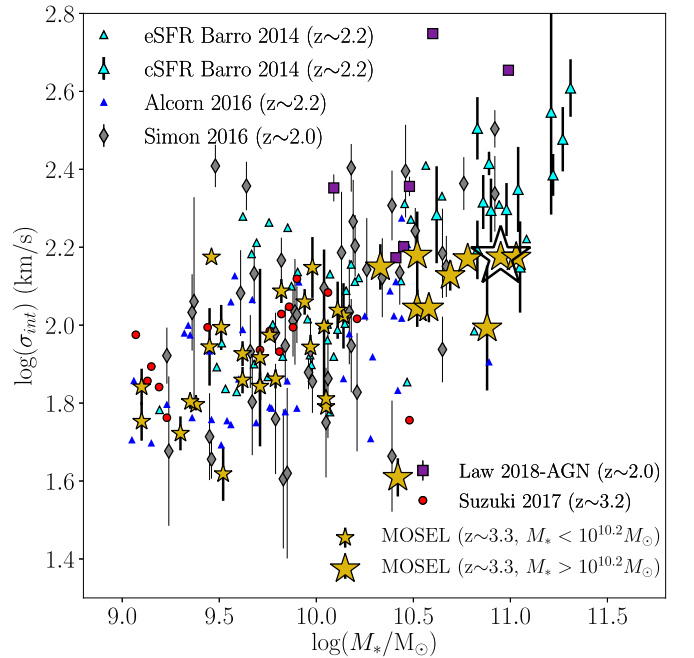**Figure 4.** Distributions of the integrated velocity dispersion ($\log(\sigma_{int})$) vs. stellar mass for the MOSEL galaxies (gold stars). The small and large gold stars correspond to the two subgroups identified using the k-Means clustering algorithm separated at a stellar mass of $M_* = 10^{10.2}M_\odot$. The big open star corresponds to a galaxy with broad emission features indicative of an AGN. We compare the MOSEL sample with SFGs at $z \sim 2$ from Barro et al. (2014), Alcorn et al. (2016), and Simons et al. (2016). Additionally, we compare with SFGs at $z \sim 3$ from Suzuki et al. (2017) and AGNs at $z \sim 2$ from Law et al. (2018).

cut-off $\log(M_*/M_\odot) = 10.2$ identified by the k-Means algorithm is similar to the turnover stellar mass in the stellar mass function at $z > 2.0$ (Davidzon et al. 2017). In the rest of the paper, we use the $\log(M_*/M_\odot) = 10.2$ cut-off to separate galaxies into low and high stellar mass bins.

3.1.2. Comparison with z > 2 Samples from the Literature

We compare the kinematic properties of MOSEL galaxies with other slit-based studies at $z \sim 2.0$ (Figure 4; Barro et al. 2014; Alcorn et al. 2016; Simons et al. 2016; Suzuki et al. 2017). We select the Simons et al. (2016) and Barro et al. (2014) samples because they cover the full stellar mass range of our MOSEL sample. From Barro et al. (2014) we combine samples of both compact and extended SFGs because they exhibit a similar relation between the stellar mass and $\log(\sigma_{int})$.

To derive $\log(\sigma_{int})$ for the Simons et al. (2016) sample, we add the inclination-uncorrected rotation velocity and intrinsic velocity dispersion in quadrature. Although our derived $\log(\sigma_{int})$ from the Simons et al. (2016) sample does not equal the observed $\log(\sigma_{int})$, we infer from the rotational model that the difference would be smaller than $20 \, km \, s^{-1}$, significantly smaller than our measurement errors. We also compare with the Alcorn et al. (2016) sample, which extends up to $\log(M_*/M_\odot) \leqslant 10.5$. The stellar masses for all comparison samples are derived using FAST (Kriek et al. 2009).

We use the Python package Lmfit (Newville et al. 2016) to fit a linear relation of the form $\log(\sigma_{int}) = A + B \times \log(M_*/M_\odot)$ to the stellar mass and $\log(\sigma_{int})$ distribution for the various samples after running an iterative 2.5σ outlier rejection. Table 1 shows the best-fit parameters of the linear relation for various comparison samples. The quoted uncertainties in Table 1 are derived from the
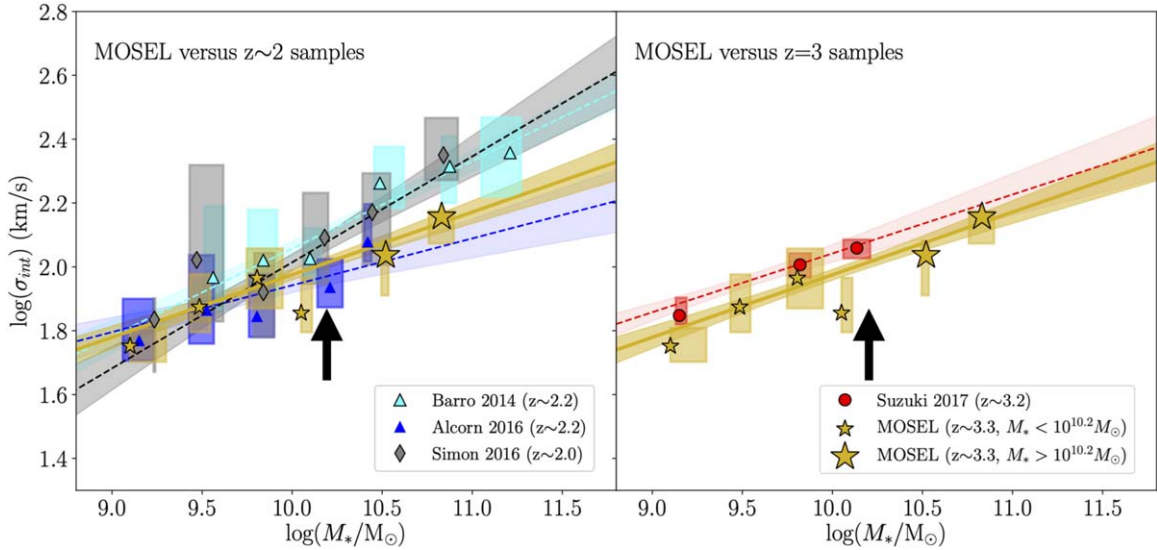
Figure 5. The integrated velocity dispersion ($\log(\sigma_{int})$) for the MOSEL galaxies (gold stars) binned in stellar mass in comparison with the samples at $z \sim 2$ (left) and $z > 3$ (right). The color scheme is the same as in Figure 4. The symbols and the shaded rectangles correspond to the median and the 25th to 75th percentile in $\log(\sigma_{int})$ and stellar mass after bootstrapping, respectively. The dashed lines represent the best-fit linear relations between M_* and $\log(\sigma_{int})$ for the respective samples. Massive galaxies with $\log(M_*/M_\odot) > 10.2$ (identified by the black arrow) from our MOSEL survey have lower $\log(\sigma_{int})$ compared to galaxies of similar stellar masses at $z \sim 2$.

Table 1
Best Least-squares Linear Fits to the Integrated Velocity Dispersion and Stellar Mass Distribution for $z > 2$ Observations

Sample	$\log(\sigma_{int})$ $(km\ s^{-1})^a$	Slope[b]	N^c	$\log(M_{dyn}/M_\odot)^a$
Barro et al. (2014), $z \sim 2.0$	1.74 ± 0.04	0.31 ± 0.03	53	9.46 ± 0.08
Barro et al. (2014), $\log(M_*/M_\odot) < 10.2$	1.91 ± 0.10	0.12 ± 0.1	30	9.52 ± 0.06
Barro et al. (2014) $\log(M_*/M_\odot) > 10.2$	1.70 ± 0.20	0.32 ± 0.1	23	9.21 ± 0.07
Alcorn et al. (2016), $z \sim 2.0$	1.80 ± 0.05	0.15 ± 0.05	41	9.25 ± 0.05
Alcorn et al. (2016), $\log(M_*/M_\odot) < 10.2$	1.80 ± 0.06	0.14 ± 0.08	30	9.41 ± 0.05
Alcorn et al. (2016), $\log(M_*/M_\odot) > 10.2$	1.94 ± 0.48	0.05 ± 0.32	11	9.14 ± 0.13
Alcorn et al. (2016), size evolution to $z = 3$	1.65 ± 0.05	0.26 ± 0.05	41	9.14 ± 0.05
Simons et al. (2016), $z \sim 2.0$	1.68 ± 0.07	0.33 ± 0.06	48	$\cdots$
Suzuki et al. (2017), $z \sim 3.0$	1.86 ± 0.03	0.17 ± 0.04	17	$\cdots$
MOSEL (this work), $z \sim 3.0$	1.78 ± 0.04	0.19 ± 0.03	34	$\cdots$
MOSEL (this work, $\log(M_*/M_\odot) < 10.2$)	1.74 ± 0.06	0.23 ± 0.07	24	9.39 ± 0.08
MOSEL (this work, $\log(M_*/M_\odot) > 10.2$)	2.06 ± 0.21	0.03 ± 0.11	10	8.75 ± 0.19

Notes.
[a] At $\log(M_*/M_\odot) = 9$ from the best linear fit.
[b] Slope of the best-fit relation of the form $\log(\sigma_{int}) = A + B^*\log(M_*/M_\odot)$.
[c] Number of objects used for the linear fit.

covariance matrix, which are consistent within 1σ to the uncertainties derived via bootstrapping. We find that massive galaxies ($\log(M_*/M_\odot) > 10.2$) at $z \sim 3$ have lower $\log(\sigma_{int})$ compared to galaxies of similar stellar masses at $z \sim 2$.

We bin the $\log(\sigma_{int})$ measurements for the MOSEL and various comparison samples in stellar mass (Figure 5). We require the stellar mass bins to have at least two galaxies in the respective sample. For each sample, we create 100 realizations for all galaxies in a particular stellar mass bin by perturbing the data points according to their uncertainties. We estimate a median and the area corresponding to the 25th to 75th percentile in the stellar mass and $\log(\sigma_{int})$ for each stellar mass bin.

The $\log(\sigma_{int})$ and stellar mass distribution for the low mass MOSEL sample ($\log(M_*/M_\odot) < 10.2$) is consistent with other studies at $z \sim 2$ (Figure 5, left panel). The SFGs from

Suzuki et al. (2017) have nearly 0.1 dex higher $\log(\sigma_{int})$ compared to the MOSEL sample (Figure 5, right panel). We suspect that the selection of galaxies via narrowband imaging biases the Suzuki et al. (2017) sample toward the high specific star formation rate (sSFR) galaxies. An intrinsic bias toward high sSFR might result in the selection of galaxies with high intrinsic velocity dispersion (Übler et al. 2019), and in turn high $\log(\sigma_{int})$.

Figure 5 shows that the MOSEL galaxies with $\log(M_*/M_\odot) > 10.2$ have lower $\log(\sigma_{int})$ compared to the same stellar mass galaxies $z \sim 2.0$. We cannot compare the $\log(\sigma_{int})$ measurements for the massive MOSEL galaxies with the Suzuki et al. (2017) sample because they only have one galaxy with $\log(M_*/M_\odot) > 10.0$. We combine the integrated velocity dispersion measurements for massive galaxies ($\log(M_*/M_\odot) > 10.2$) in Barro et al. (2014) and Simons et al. (2016), and bootstrap to estimate a median $\log(\sigma_{int})$ of massive galaxies at $z \simeq 2$. After bootstrapping the
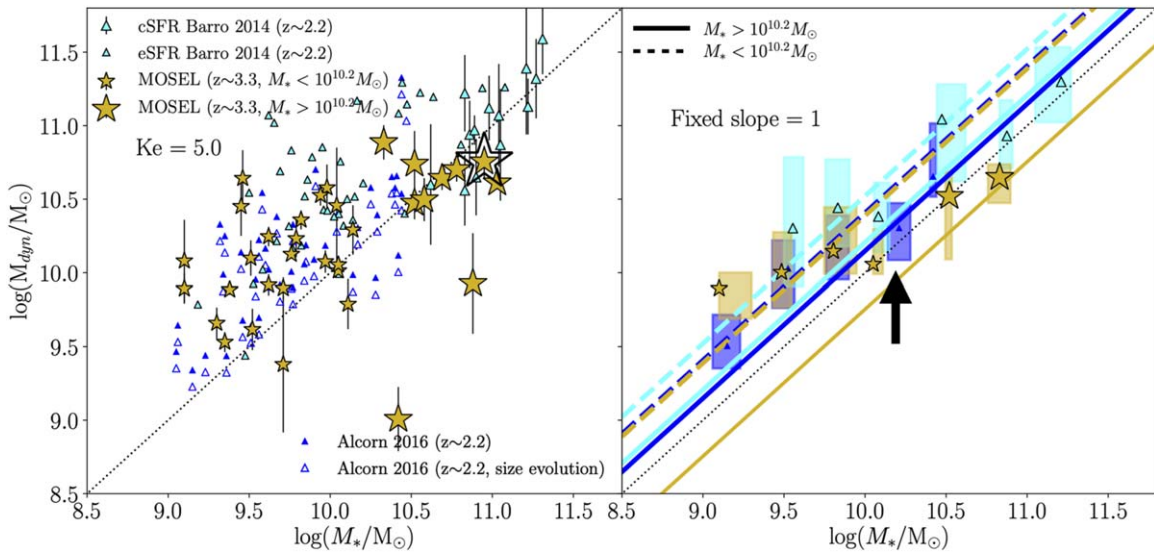
Figure 6. Comparison between the dynamical mass and stellar mass in the left panel. The color scheme is the same as in Figure 4. The open blue triangles in the left panel correspond to the size evolution corrected dynamical mass estimates for the Alcorn et al. (2016) sample. The right panel shows the dynamical masses after stellar mass binning for each sample. The symbols and shaded rectangles correspond to the median and 25th to 75th percentile. The colored dashed and solid lines in the right panel correspond to the best-fit dynamical mass for galaxies with $\log(M_*/M_\odot) < 10.2$ (identified by the black arrow) and $\log(M_*/M_\odot) > 10.2$, respectively, for each sample. We find that massive galaxies at $z \sim 3.0$ have a lower dynamical mass compared to $z \sim 2$ galaxies of similar stellar masses.

$\log(\sigma_{\rm int})$ for the massive MOSEL galaxies, we estimate that massive MOSEL galaxies have nearly $56 \pm 21 \, {\rm km \, s^{-1}}$ lower integrated velocity dispersion compared to the similar stellar mass galaxies at $z \sim 2.0$.

3.1.3. Contamination from AGN and Mergers

To identify the role of AGNs, we compare our measurements with a sample of six narrow-line AGNs from Law et al. (2018). The integrated velocity dispersion of the Law et al. (2018) sample shows a large scatter, where only two galaxies have $\sigma_{\rm int} > 500 \, {\rm km \, s^{-1}}$. The Barro et al. (2014) sample might also have some contribution from AGNs, because some of their compact star-forming galaxies exhibit broad emission features with X-ray emission. To remove AGNs from the MOSEL sample, we use X-ray, radio, and infrared emission catalogs from Cowley et al. (2016). One of our massive MOSEL galaxies shows a clear sign of broad emission, indicative of either an AGN, shocks, or outflows (Figure 10). We do not rule out contamination from narrow-line AGNs in our massive galaxy sample.

Our results cannot be explained by the higher probability of misclassification of mergers as rotating disks at $z \sim 3.0$ compared to $z \sim 2.0$ (Hung et al. 2015). We do find some indications of extended diffuse components for some galaxies (Figure 11), indicative of mergers. However, misclassified mergers as rotating disks at $z \sim 3.0$ would result in a relatively higher observed $\log(\sigma_{\rm int})$ for galaxies at $z \sim 3.0$, in contrast to our result.

We speculate that the lower integrated velocity dispersions we find for massive galaxies at $z > 3$ as compared to similar mass galaxies at $z \sim 2$ indicates that either the rotation velocity or intrinsic velocity dispersion decreases for massive galaxies from redshift 2 to 3 (See Section 5).

3.2. Dynamical Mass Analysis

Figure 6 shows the comparison between the dynamical mass and the stellar mass for MOSEL galaxies. To measure

dynamical masses, we use the virial theorem

$$M_{\rm dyn} = Ke \frac{\sigma_{\rm int}^2 R_e}{G} \quad (1)$$

where R_e is the effective radius and Ke is the virial factor. The effective radius was measured using GALFIT on *HST*-F160W imaging (Section 2.4). The value of Ke depends on the mass profile, the ratio of velocity dispersion to the rotation, and the shape of the overall gravitational potential (Courteau et al. 2014). The virial factor can range between 2 and 10 depending on the overall structure of the galaxy (Maseda et al. 2013; van de Sande et al. 2013).

To consistently compare with studies at $z > 2$, we choose a virial factor of $Ke = 5$, which is typically used for dispersion dominant disks at high redshifts (Barro et al. 2014; Maseda et al. 2014; Price et al. 2015; Alcorn et al. 2016). The choice of the virial factor would change our dynamical mass estimates but does not affect the main conclusion of this paper. We compare the dynamical mass estimates for MOSEL galaxies with the Alcorn et al. (2016) and Barro et al. (2014) samples because they provide effective radii or dynamical masses for their sample. We determine the offset between the dynamical mass and stellar mass for various observational studies by performing a linear fit with 2.5σ outlier rejection at a fixed slope of 1 (Table 1). For a reliable estimate of effective radii, we only select MOSEL galaxies where residuals after surface brightness profile fitting via GALFIT are less than 20%.

We estimate that massive galaxies ($\log(M_*/M_\odot) > 10.2$) in our MOSEL sample have nearly 0.4 dex lower dynamical mass compared to galaxies of similar stellar masses at $z \sim 2$. The relation between dynamical mass and stellar mass for the low mass MOSEL sample ($\log(M_*/M_\odot) < 10.2$) is consistent within 1σ errors to other studies at $z > 2.0$. The two massive galaxies with unphysical dynamical masses in our sample are extremely compact (see Figure 3), and one of them has an integrated velocity dispersion close to the spectral resolution limit of MOSFIRE ($\sim 32 \, {\rm km \, s^{-1}}$). By analyzing the inclination of

massive galaxies on the sky from GALFIT, we rule out a preference toward face-on galaxies in our MOSEL sample (Figure 11).

The stellar mass to effective radii distribution of our MOSEL sample is similar to the Barro et al. (2014) and Alcorn et al. (2016) samples (Figure 3). The effective radii of our galaxies are consistent within 1σ errors to the stellar mass versus size relation derived by Allen et al. (2016) using the ZFOURGE data for galaxies at $z = 3$–4 (Figure 3). We estimate that a simple size evolution of galaxies between $z = 2$ to $z = 3$ would result in the observation of a 0.1 dex lower dynamical mass measurement for galaxies at $z = 3$ (open blue triangles in Figure 6, left panel). However, an offset of 0.1 dex is insufficient to explain the ~0.5 dex lower dynamical mass of massive galaxies at $z \sim 3$ compared to galaxies of similar stellar masses at $z \sim 2$. We speculate there is a shift in the evolutionary pathway of massive galaxies between $z = 2$–3.

3.3. Star Formation Histories of MOSEL Galaxies

The kinematic state of the gas is modulated by the SFH of the galaxy and the gas inflows/outflows. We use a Python-based SED fitting code PROSPECTOR to recover the SFHs of MOSEL galaxies (Leja et al. 2017, 2019a). The extensive ZFOURGE photometry (Straatman et al. 2016) provides us with fluxes in nearly 30 photometric bands for MOSEL galaxies.

Figure 7 shows the recovered SFHs of the massive and low mass galaxies of our MOSEL sample in comparison with the ZFIRE sample (Nanayakkara et al. 2016). We have normalized the SFR to the recovered stellar mass of each galaxy. The stellar mass estimates from PROSPECTOR are nearly 0.5 dex higher than the stellar masses estimated using FAST (Kriek et al. 2009) in the ZFOURGE survey, similar to the Cohn et al. (2018) observation. The stellar mass difference between PROSPECTOR and FAST is due to the older stellar populations inferred by the nonparametric SFHs. Parametric SFH fits would be biased toward the younger stellar ages to explain the UV luminosity of galaxies. Thus, the contribution of the older stellar population to the total mass will not be correctly constrained (Leja et al. 2019b). For consistency, we use the stellar mass estimates from FAST to separate galaxies into the two mass bins.

The MOSEL and ZFIRE samples are derived from the ZFOURGE surveys, allowing a consistent measurement of SFHs for both samples. We again separate the ZFIRE and MOSEL galaxies into two mass bins at $\log(M_*/M_\odot) = 10.2$. To estimate the median and scatter in SFHs for each sample, we generate 1000 samples for each galaxy using the distribution of the posterior for each parameter. For each galaxy sample, we combine all randomly generated samples in each time bin and calculate the 16th, 50th, and 84th percentiles. The median and scatter in sSFR in the sixth time bin (~1.4–1.9 Gyr) is calculated without bootstrapping because it is not an independent variable in PROSPECTOR.

Massive galaxies ($\log(M_*/M_\odot) > 10.2$) in our MOSEL sample show either constant or declining SFHs, whereas low mass galaxies ($\log(M_*/M_\odot) < 10.2$) have rising SFHs until 50 Myr ago. In contrast, there is no significant difference in SFHs of the low and high mass galaxies at $z \sim 2$ from ZFIRE observations. Massive galaxies at $z > 3$ only assemble ~30% of their stellar mass in the past 500 Myr, whereas galaxies of similar stellar masses at $z \sim 2.0$ assemble more than ~45% of their stellar mass in the past 500 Myr. The low mass galaxies in the both MOSEL

and ZFIRE surveys assemble ~65% of their stellar mass in the past 500 Myr. Figure 7 shows that massive galaxies at $z > 3$ have nearly flat median SFHs, in contrast to the rising median SFHs of massive galaxies at $z = 2$. We cannot derive statistically significant conclusions about the difference in the SFHs because of our limited sample size and large uncertainties.

Nearly constant SFHs of the massive galaxies ($\log(M_*/M_\odot) > 10.2$) at $z > 3.0$ suggests their relatively quiet evolution without a sudden influx of gas or mergers. We find that sSFRs drops in the 0–50 Myr time bin irrespective of the sample, probably because nonparametric SFHs are better determining older stellar populations with ages >100 Myr (Leja et al. 2019b). A larger sample of galaxies and better photometric sampling in infrared bands for galaxies at $z > 2.0$ is required to improve constraints on SFHs.

4. Mass Assembly in Cosmological Simulations

Using slit-based spectroscopic observations of galaxies at $z \sim 3.0$ in the MOSEL survey, we find that massive galaxies ($\log(M_*/M_\odot) > 10.2$) have 56 ± 21 km s^{-1} lower integrated velocity dispersion compared to galaxies in a similar stellar mass range at $z \sim 2.0$ (Figure 4). We speculate that a lower dynamical mass for massive galaxies at $z = 3$ compared to galaxies at $z = 2$ could be responsible for their low velocity dispersion.

We use a cosmological hydrodynamical simulation, IllustrisTNG (Marinacci et al. 2018; Naiman et al. 2018; Nelson et al. 2018; Pillepich et al. 2018; Springel et al. 2018) to understand the evolution of the dynamical mass of galaxies. We use the ~(100 Mpc)^3 volume (TNG100) simulation, because it has sufficient volume to produce a statistically significant sample of massive galaxies at $z > 3$ (as opposed to TNG50). TNG100 also has sufficient numerical resolution to reliably constrain the properties of galaxies with $M_* \sim 10^9 M_\odot$.

TNG100 has a baryonic mass resolution of $m_b = 9.4 \times 10^5$ h^{-1}, where m_b is the baryonic mass per particle. Selecting galaxies from TNG100 at $\log(M_*/M_\odot) > 9$ results in at least 1000 stellar particles per galaxy, minimizing the numerical uncertainties. To identify the progenitors of each selected galaxy, we track them back in time using the merger tree catalogs generated using the Rodriguez-Gomez et al. (2015) technique. An additional cut of SFR > 0 is imposed while selecting galaxies at any redshift epoch because we aim to compare with kinematic measurements via emission lines that are intrinsically biased toward SFGs.

4.1. Disk-size Comparison between Observations and Simulations

To compare the dynamical mass between simulations and observations, we use the total mass enclosed within a stellar half-mass radius ($R_{\rm halfmass}^*$) for simulated galaxies. Similar to Genel et al. (2018), $R_{\rm halfmass}^*$ is defined as the three-dimensional (3D) radius enclosing 50% of the mass of all evolving stellar particles (stars plus stellar remnants) assigned to the galaxy by the SUBFIND algorithm. Genel et al. (2018) show that the $R_{\rm halfmass}^*$ is consistent within 1σ scatter to the 2D projected sizes in the r-band across all stellar masses for both main-sequence and quenched galaxies. Although, the 3D $R_{\rm halfmass}^*$ is nearly 0.1–0.2 dex higher than the two-dimensional half-light radius for simulated galaxies with $\log(M_*/M_\odot) < 10.0$.

Figure 8 shows the relation between $R_{\rm halfmass}^*$ and stellar mass for the TNG100 galaxies across two redshift snapshots in

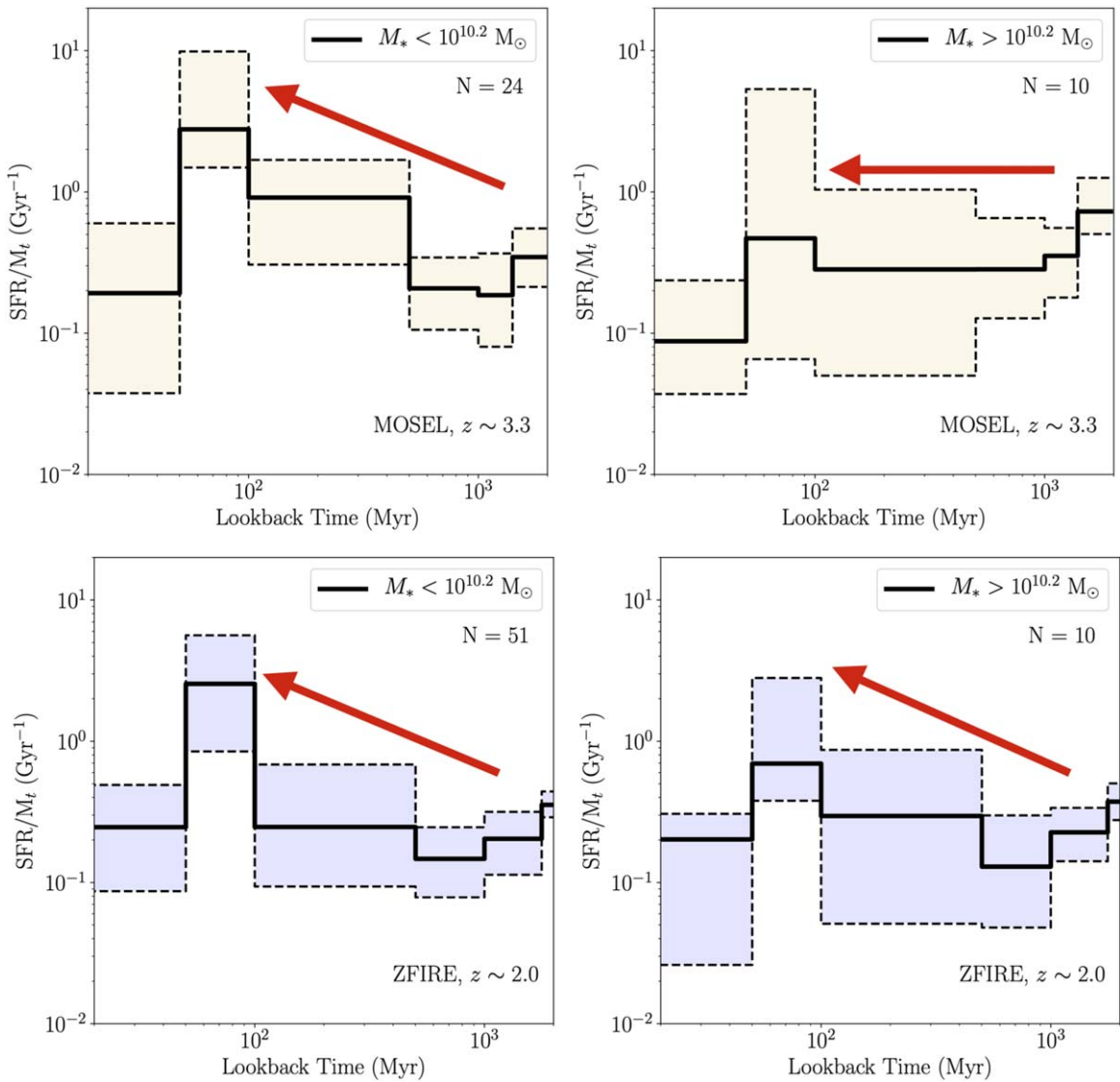**Figure 7.** Star formation history of the low (log($M_*/M_\odot$) < 10.2; left) and high mass galaxy (log($M_*/M_\odot$) > 10.2; right) samples in the MOSEL (top) and ZFIRE (bottom) surveys using PROSPECTOR (Leja et al. 2017, 2019a). The solid black line and the shaded region in each panel represent the median and 16–84 percentile regions, respectively. The red arrow in each panel shows the qualitative slope of SFHs in the respective samples. The massive MOSEL galaxies have flat/declining SFHs in contrast to the SFHs in other samples.

comparison to the stellar mass–size relation of our MOSEL galaxies. In simulations, the relation between $R^*_{\rm halfmass}$ and the stellar mass remains consistent across $z = 2$–3 within 1σ scatter. We do find an increased scatter in the $R^*_{\rm halfmass}$ at the massive end at $z = 2$ in simulations.

Similar to Genel et al. (2018), we find that the effective radii of galaxies in observations are slightly smaller than the $R^*_{\rm halfmass}$ in simulations across both redshift intervals at the low mass end. Inherent observational bias against the extended low-surface brightness region, projection effects, and uncertainties in the mass-to-light ratio, especially at high redshift, might be responsible for the discrepancy in the galaxy size between observations and simulations (Bernardi et al. 2017; Genel et al. 2018).

4.2. Dynamical Mass Evolution

Figure 9 shows a comparative evolution of the dynamical mass in observations and simulations. We remeasure the dynamical mass of MOSEL galaxies and the Alcorn et al. (2016)

sample at $z \sim 2.0$ using Equation (1) but with a virial factor $Ke = 2.5$ to estimate the enclosed dynamical mass within the effective radii (Courteau et al. 2014).

In simulations, we define dynamical mass as the total mass (dark + baryonic matter) enclosed within $R^*_{\rm halfmass}$. We bin the data into ten bins of equal stellar mass. Due to the small number of massive galaxies in TNG100, we only select stellar mass bins that have more than five galaxies. We find a consistent relation between the dynamical mass versus the stellar mass relation of simulated galaxies across $z = 2$–3, at least for log($M_*/M_\odot$) < 10. We find a systematic upturn in the dynamical mass of simulated galaxies at the massive end. The mean dynamical mass of simulated galaxies with log($M_*/M_\odot$) > 10.0 increases by roughly 0.1 dex between $z = 2$–3.

Observational measurements of dynamical mass from integrated spectra are riddled with unknowns such as the mass-to-light ratio, projection effects, kinematic profiles, and S/N, making a direct comparison of dynamical masses from observations and simulations difficult. We find that the dynamical mass of
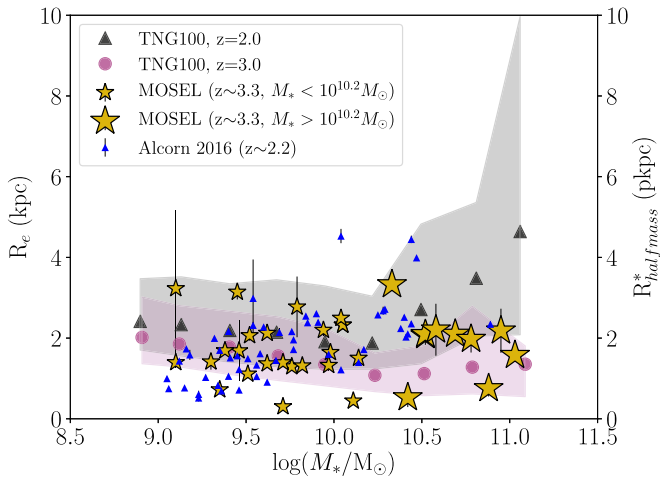
Figure 8. Comparison between *HST*-F160W effective radii (R_e) from observations and $R^*_{halfmass}$ from the TNG100 simulation as a function of the stellar mass. The large and small golden stars correspond to the MOSEL galaxies with $\log(M_*/M_\odot) > 10.2$ and $\log(M_*/M_\odot) < 10.2$, respectively. The pink circles and shaded region represent the 50th, 16th, and 84th percentiles in the $R^*_{halfmass}$ from TNG100 at $z = 3.0$. Similarly, the black triangles and gray shaded region represent the $R^*_{halfmass}$ at $z = 2.0$ in TNG100.

simulated galaxies at $z = 3$ is systematically $\sim$0.4 dex higher than for the massive galaxies in our MOSEL sample. The lower dynamical mass of massive MOSEL galaxies compared to simulated galaxies can be due to our choice of a virial factor that is true for only disky galaxies and would underestimate the dynamical mass of compact massive galaxies with high Sérsic indices (Cappellari et al. 2006; Courteau et al. 2014).

The Alcorn et al. (2016) sample at $z \sim 2.0$ only extends up to $\log(M_*/M_\odot) < 10.5$, so we cannot compare the dynamical mass estimates of the massive MOSEL galaxies with galaxies at $z = 2$. The $R^*_{halfmass}$ for simulated galaxies is nearly two times larger than 2D projected half-light radii for observed galaxies with $\log(M_*/M_\odot) < 9.5$ (Figure 8), which might be responsible for the $\sim$0.5 dex higher dynamical mass of low mass simulated galaxies compared to the observations. Within the limitation of our observational data, we do not find any systematic difference between the dynamical mass of the MOSEL sample at $z > 3.0$ and the ZFIRE sample from Alcorn et al. (2016) at $z \sim 2$. A larger sample of photometric and spectroscopic data between $z = 2-4$ is required to observationally identify changes in the dynamical mass of galaxies between $z = 2-4$.

4.3. In Situ versus Ex Situ Growth

We use the Rodriguez-Gomez et al. (2016) stellar assembly catalog to estimate the evolution of the ex situ stellar mass fraction. Rodriguez-Gomez et al. (2016) defines the ex situ stellar mass fraction as the fractional amount of stellar mass for a galaxy that is contributed by the stars formed in other galaxies, which were subsequently accreted in the galaxy. The ex situ stellar mass fraction gives us a handle on the amount of stellar mass growth from accretion versus the in situ star formation.

The right panel in Figure 9 shows the evolution in the ex situ stellar mass fraction with redshift. At each redshift epoch, we select simulated galaxies with nonzero SFRs and split them into two stellar mass bins at $\log(M_*/M_\odot) = 10.2$ to match with our observations. In the low stellar mass bin, we only select galaxies with $\log(M_*/M_\odot) > 9.0$ to minimize numerical uncertainties. We calculate the 50th, 16th, and 84th percentiles in the ex situ stellar mass fraction for the two stellar mass bins.

Figure 9 clearly shows a systematic increase in the ex situ stellar mass fraction of massive simulated galaxies. The low mass galaxies accrete roughly 6% of their stellar mass from other galaxies, and the fraction remains unchanged until $z = 1.0$. In contrast, massive simulated galaxies accrete $\sim$6.8% of their stellar mass from other galaxies until $z \sim 3.5$, which subsequently increases rapidly. The median ex situ stellar mass fraction for massive galaxies changes from $\sim$9% at $z = 3$ to $\sim$13% at $z = 2$ and reaches to about 17% by $z = 1$. The increased scatter in the ex situ stellar mass fraction for massive galaxies toward lower redshift might be driven by the absolute increase in the total number of massive galaxies at low redshifts.

Our choice of the stellar mass cut is nearly equal to M^* for the SFG population at $z = 2.5-3$, where M^* is the turnover mass in the stellar mass function (Davidzon et al. 2017). Changing the stellar mass cut-off to $\log(M_*/M_\odot) = 10.0$ pushes the redshift at which the ex situ stellar mass fraction starts to rise to slightly lower redshifts without significantly altering the systematic trend. Our result is consistent with the Rodriguez-Gomez et al. (2016) analysis, who use the original Illustris simulation to find that the transition from in situ to ex situ stellar mass growth occurs only for the most massive galaxies at $z \approx 1.0$.

We suspect that the stellar mass growth via ex situ processes might be responsible for the increase in the integrated velocity dispersion of massive galaxies between $z = 3.0$ to $z = 2.0$ (see Section 5 for further discussion).

5. Discussion

By measuring the [O III] emission line profile from MOSFIRE observations, we find that massive galaxies ($\log(M_*/M_\odot) > 10.2$) at $z > 3$ have nearly 56 ± 21 km s^{-1} lower integrated velocity dispersion than similar stellar mass galaxies at $z \sim 2$ (Figure 4). We also find that massive galaxies at $z > 3.0$ have either flat or declining SFHs, while in contrast galaxies of similar stellar mass at $z \sim 2.0$ have slightly rising SFHs (Figure 7). The integrated velocity dispersion represents a combination of the rotation velocity and intrinsic velocity dispersion of galaxies, thus giving us a handle on both the kinematic properties of gas and the total mass budget of galaxies. In the following subsections, we try to disentangle the evolution of the intrinsic velocity dispersion from the mass assembly history of galaxies to explain our observations.

5.1. Kinematics of Gas and SFHs

Large surveys such as KMOS^{3D} have shown a significant evolution in the kinematics of ionized gas between $z = 1-3$ (Wisnioski et al. 2015). Both local and high-redshift galaxies show a correlation between the intrinsic velocity dispersion of gas and their star formation rate, albeit with a significant secondary dependence on other galaxy properties such as gas fraction (Krumholz & Burkhart 2016). Internal secular processes such as evolving gas reservoirs, higher star formation rate, and gravitational instabilities introduced by the gas accretion and outflows drive the higher intrinsic velocity dispersion of high-redshift galaxies (Newman et al. 2013; Krumholz & Burkhart 2016; Wiseman et al. 2017; Davies et al. 2019; Martin et al. 2019; Zabl et al. 2019).

The cosmic star formation density peaks at $z \sim 2.0$ (Madau & Dickinson 2014). The declining cosmic SFR density at $z > 2$ could lead to a decline in the intrinsic velocity dispersion
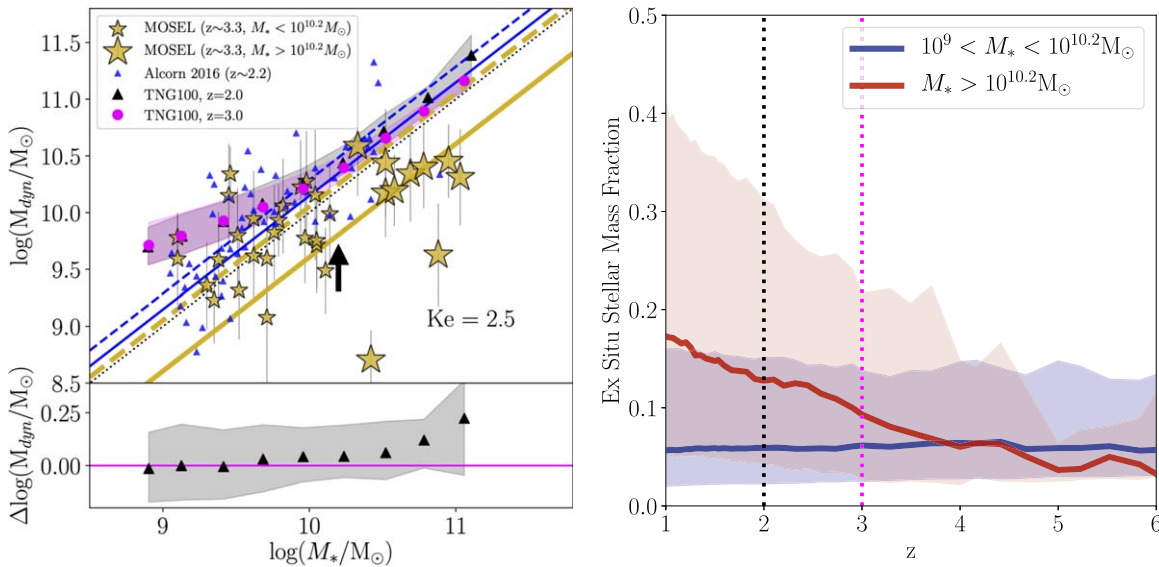
Figure 9. Left panel: comparison between the dynamical to stellar mass relation in observations and simulations. The color scheme and symbols are the same as Figure 8. The black dotted line is the one-to-one line. The colored dashed and solid lines represent the average offset in the dynamical mass of low and high mass (split at $\log(M_*/M_\odot) = 10.2$, pointed to by the black arrow) galaxies in the respective samples from the one-to-one line. The bottom panel shows the change in the dynamical mass at a fixed stellar mass between $z = 2$–3, showing the ~ 0.1 dex increase in the dynamical mass at $z = 2$ for massive galaxies. Right panel: the ex situ stellar mass fraction (accreted) with respect to redshift for low mass ($9.0 < \log(M_*/M_\odot) < 10.2$, blue) and high mass samples ($\log(M_*/M_\odot) > 10.2$, red) in the TNG100 simulation. The solid line and shaded region represent the median and 16th and 84th percentiles, respectively. The pink and black dotted lines mark the redshift snapshots of $z = 3$ and $z = 2$, respectively. The ex situ stellar mass fraction increases sharply below $z < 3.5$ for massive galaxies.

of galaxies at $z > 2.0$. Saintonge et al. (2013) also find evidence of a flattening or decrease in the cold gas fraction for galaxies at $z > 2.8$, which could translate into lower intrinsic velocity dispersion. Current observational studies do not show any conclusive evidence of a decline in the intrinsic velocity dispersion of massive galaxies at $z > 2.0$ (Turner et al. 2017; Übler et al. 2019).

Most integral field spectroscopic observations have small numbers of galaxies at $z > 3$ especially at $\log(M_*/M_\odot) > 10.0$ (Gnerucci et al. 2011; Wisnioski et al. 2015; Girard et al. 2018). With a sample of 11 galaxies at $z > 3$ in the $\log(M_*/M_\odot) = 9.0$–11.0 range, Gnerucci et al. (2011) find the intrinsic velocity dispersion of galaxies is $\sim 60\,\mathrm{km\,s^{-1}}$. By combining data from various observations between $z = 1$–3.5, Wisnioski et al. (2015) find that the intrinsic velocity dispersion of galaxies with $\log(M_*/M_\odot) > 10.5$ increases from $\sim 50\,\mathrm{km\,s^{-1}}$ at $z = 2$ to $\sim 70\,\mathrm{km\,s^{-1}}$ at $z \sim 3$. Similarly, Turner et al. (2017) find that galaxies at $z > 3$ have nearly $70\,\mathrm{km\,s^{-1}}$ intrinsic velocity dispersion. However, a monotonic rise in the intrinsic velocity dispersion with redshift is opposite to our observation of a lower integrated velocity dispersion for galaxies at $z > 3$ compared to galaxies of similar stellar masses at $z \sim 2.0$.

Girard et al. (2018) analyze the kinematics of 24 gravitationally lensed galaxies at $z = 1.4$–3.5 as a function of stellar mass and redshift. They find no significant evolution in the intrinsic velocity dispersion of low mass galaxies ($\log(M_*/M_\odot) < 10$) between $z \sim 3.0$ to $z \sim 2.0$, similar to our $\log(\sigma_{int})$ measurements for the low mass galaxy sample (Figure 4). By separating galaxies into two stellar mass bins at $\log(M_*/M_\odot) = 10.2$, Girard et al. (2018) find $\sim 15\,\mathrm{km\,s^{-1}}$ lower intrinsic velocity dispersion for massive galaxies compared to the low mass galaxies. They suspect irregular sampling might be responsible because the average redshift of their low mass sample is $z \sim 3.1$, while in contrast the average redshift of the high mass sample is $z \sim 2.4$.

In lieu of any conclusive evidence that the intrinsic velocity dispersion of massive galaxies declines or steadily rises between $z = 2$–4, we cannot rule out a lower intrinsic velocity dispersion of massive galaxies at $z > 3.0$ compared to galaxies of similar stellar masses at $z \sim 2$. In the following subsection, we discuss if a difference in the mass assembly history can explain our observations.

5.2. Mass Assembly History

Kinematic properties of gas and stars are a powerful tool to understand the relative contribution of various physical processes such as monolithic collapse of gas (Eggen et al. 1962; Searle & Zinn 1978), smooth gas accretion (Fall & Efstathiou 1980), and galaxy–galaxy mergers (White & Rees 1978) to the mass assembly history of galaxies. Observational studies find an increasing role of the baryonic component in the total mass budget of galaxies at higher redshifts (Förster Schreiber et al. 2009; Gnerucci et al. 2011; Simons et al. 2016; Glazebrook et al. 2017; Straatman et al. 2017; Price et al. 2019). Übler et al. (2017) find between $z = 0.9$–2.3 the zero-point of the stellar mass Tully–Fisher relation (TFR) does not change but the baryonic TFR decreases significantly. The higher baryonic content of high-redshift galaxies at a fixed stellar mass is driven by the rising gas fraction of galaxies with redshift (Saintonge et al. 2013; Tacconi et al. 2018).

Gnerucci et al. (2011) find that the zero-point of the TFR is lower by 0.88 dex for galaxies at $z > 3.0$ compared to $z \sim 2.0$, albeit with a significant scatter. Price et al. (2019) also find that the dark matter fraction of galaxies decreases with redshift until $z \sim 3.5$. The $z > 3.0$ sample of Price et al. (2019) extends only until $\log(M_*/M_\odot) < 10.5$ compared to our $\log(M_*/M_\odot) \sim 11.0$. Within the limited sample and scatter, our massive MOSEL galaxies have ~ 0.4 dex lower dynamical mass compared to the same stellar mass galaxies at $z \sim 2$ in observations (Figure 6).

In IllustrisTNG simulations, we find a 0.1 dex increase in the dynamical mass of massive simulated galaxies at a fixed stellar mass between $z = 2$–3 (Figure 9). Observational estimates of the dynamical mass roughly follow a similar relation to simulations, albeit with a larger scatter. We suspect that not accounting for, e.g., the likely higher Sérsic index and compact structure of our massive MOSEL galaxies may account for the $\sim$0.4 dex lower dynamical mass compared to the same stellar mass galaxies from the IllustrisTNG simulation.

Our observation of a lower integrated velocity dispersion of massive galaxies at $z = 3$ compared to galaxies of similar stellar masses at $z \sim 2$ could be probing the changing rotation velocity profile of massive galaxies due to the evolving baryonic fraction. We note that the resolved kinematic observations of massive galaxies at $z > 3$ are required to confirm the changing rotation profile of galaxies. Lang et al. (2017) and Genzel et al. (2017) find a turnover in the rotation velocity of the gas in galaxies at $z \sim 2.0$. They speculate that a lower concentration of dark matter in the inner galactic disks, resulting from the ongoing dark matter assembly and asymmetric drift pressure, is responsible for the turnover in the rotation velocity profile. Teklu et al. (2018), using *Magneticum Pathfinder* simulations (Beck et al. 2016), show that even after including the asymmetric drift pressure support for cold gas, almost 50% of their galaxies exhibit a turnover in their rotation curves, indicative of the low dark matter fraction in high-redshift galaxies. However, observations of resolved rotation profiles are susceptible to the variable spatial resolution and size evolution of galactic disks (Tiley et al. 2019).

We find that in the IllustrisTNG simulation, the 0.1 dex rise in the dynamical mass to the stellar mass fraction of massive galaxies at $z = 2.0$ is coupled to a rise in the ex situ stellar mass fraction. The ex situ stellar mass fraction of massive galaxies ($\log(M_*/M_\odot) > 10.2$) increases by a factor of two between $2 < z < 3.5$ (Figure 9). In contrast, the ex situ stellar mass fraction of low mass galaxies remains nearly constant.

The rising contribution of ex situ processes such as mini and minor mergers can be responsible for the nearly 0.1 dex higher dynamical mass of massive galaxies at $z = 2$ compared to $z = 3$ in simulations (Section 3.2; Hilz et al. 2013). The ex situ processes through the accretion of gas and stars can drive significant turbulence and gravitational instabilities in the galactic disks (Genel et al. 2012; Mandelker et al. 2014), which in turn can result in a higher intrinsic velocity dispersion of galaxies (Krumholz et al. 2018).

We speculate that the observation of a higher integrated velocity dispersion of massive galaxies at $z = 2.0$ compared to galaxies of similar stellar masses at $z > 3$ is probing the transition from the in situ to ex situ in the stellar mass assembly history of massive galaxies. Rising SFHs of massive galaxies at $z = 2.0$ also supports that massive galaxies at $z = 2.0$ have acquired a fresh supply of gas in the past 500 Myr (Figure 7).

6. Summary

In this work, we combine near-infrared spectroscopic observations from MOSFIRE/Keck and deep ZFOURGE photometry with IllustrisTNG simulations to analyze the mass assembly histories of galaxies at $z > 3$. Our main results are:

1. By measuring the [O III] emission profile of galaxies at $z \sim 3.3$, we find that galaxies with $\log(M_*/M_\odot) > 10.2$ have 56 ± 21 km s^{-1} lower integrated velocity

dispersion compared to galaxies of similar stellar masses at $z \sim 2.0$ (Figure 4).

2. We convert the integrated velocity dispersion into the dynamical mass of galaxies using the virial theorem and find that massive galaxies at $z > 3$ have $\sim$0.4 dex lower dynamical mass compared to galaxies of similar stellar masses at $z \sim 2$ (Figure 6).

3. We use PROSPECTOR to estimate SFHs of galaxies from the ZFIRE and MOSEL surveys and find that massive galaxies at $z > 3$ have either flat or declining SFHs until 50 Myr ago. In contrast, similar stellar mass galaxies at $z \sim 2$ show a slight peak in their SFH in the last 50 Myr (Figure 7).

4. Using IllustrisTNG simulations, we find a systematic 0.1 dex increase in the dynamical to stellar mass ratio of massive simulated galaxies ($\log(M_*/M_\odot) > 10.0$) at $z = 2$ compared to $z = 3$ galaxies (Figure 9).

5. By probing the stellar mass assembly histories of simulated galaxies, we find a rapid rise in the ex situ stellar mass fraction of massive galaxies ($\log(M_*/M_\odot) > 10.2$) at $z < 3.5$. In contrast, the ex situ stellar mass fraction of the low mass sample remains constant across cosmic time (Figure 9).

We speculate that the high integrated velocity dispersion and rising SFHs of massive galaxies at $z \simeq 2.0$ compared to galaxies of similar stellar masses at $z > 3.0$ are driven by the rising contribution of ex situ stellar mass to the total stellar mass growth of massive galaxies. However, our conclusions are limited by the low signal-to-noise ratio, limited sample size, and heterogeneous stellar mass coverage of existing data. Large spectroscopic and photometric surveys of galaxies between $z = 2$–4 with future facilities like GMT, ELT, MSE, and LSST will provide sufficient samples and depth to test this hypothesis.

Appendix

We show the MOSFIRE spectra and HST-F160W image of all massive MOSEL galaxies in Figures 10 and 11, respectively.
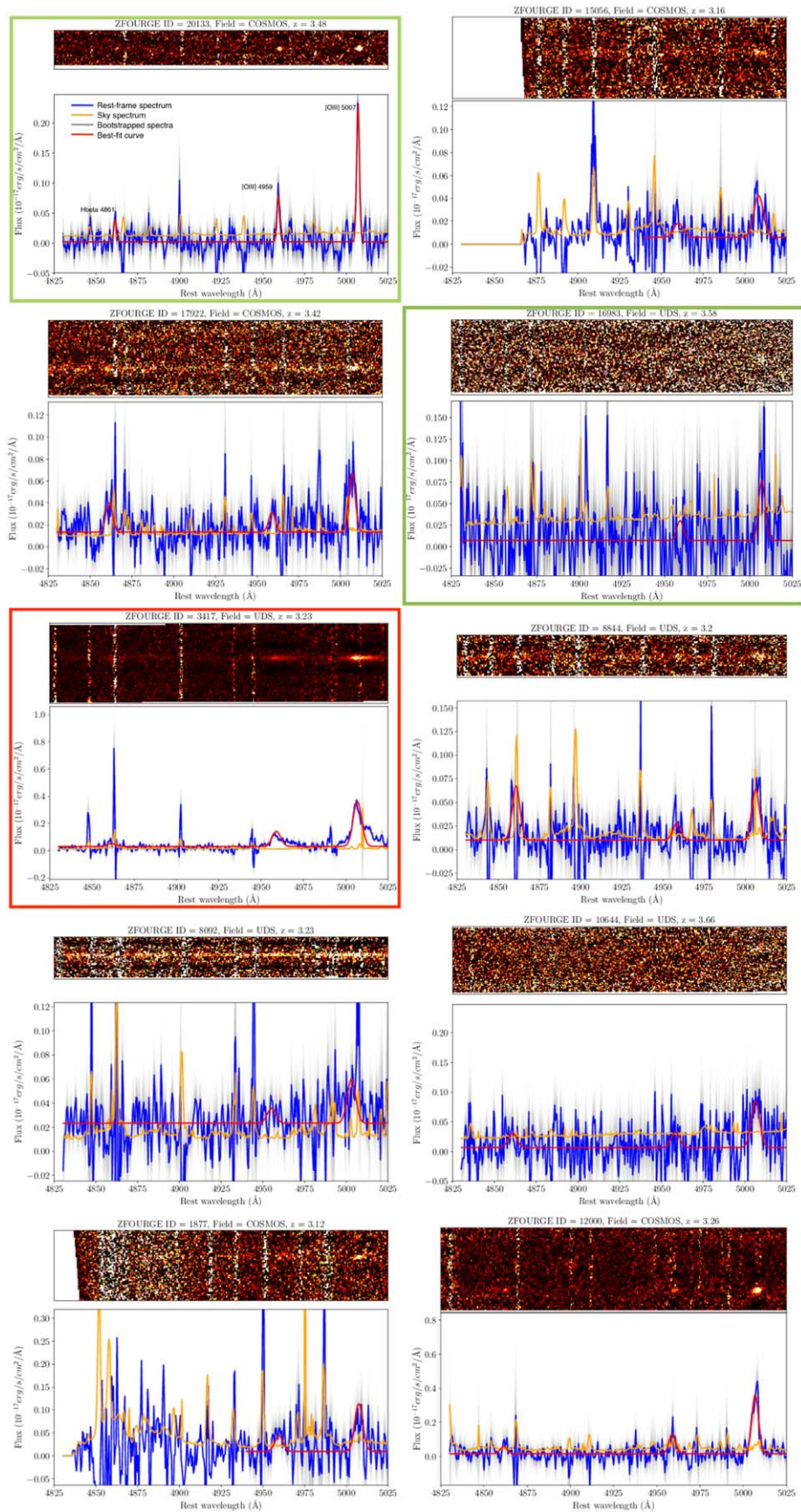
Figure 10. Same as Figure 1 but for all 10 galaxies with $\log(M_*/M_\odot) > 10.2$. Spectra of two galaxies with unphysical dynamical masses are highlighted with green boxes. The spectrum highlighted with a red box corresponds to a possible AGN contaminant.
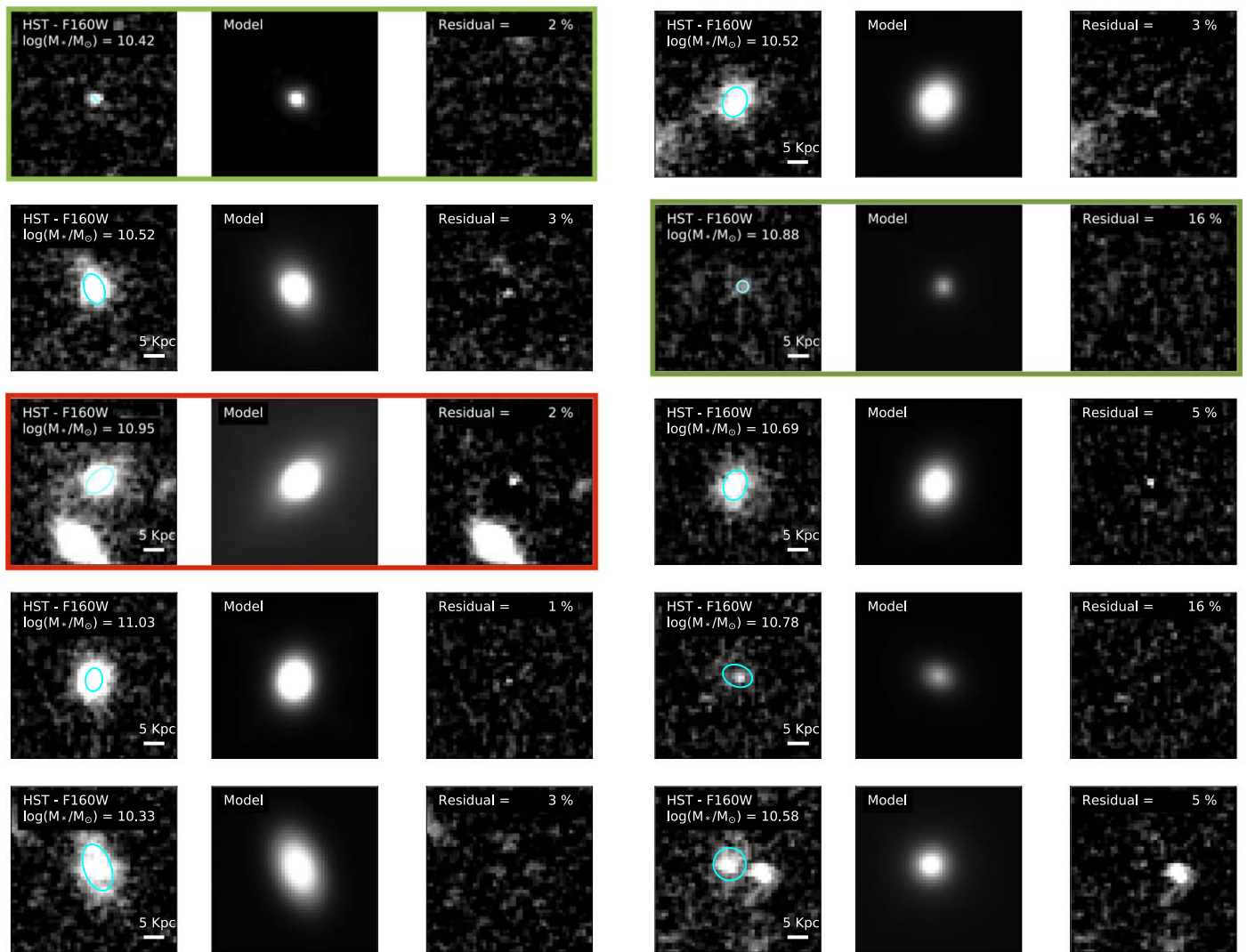
Figure 11. Same as Figure 2 but for all 10 galaxies with $\log(M_*/M_\odot) > 10.2$. The *HST*-F160W image and GALFIT models highlighted with green and red boxes correspond to galaxies with unphysical dynamical masses and a possible AGN contaminant, respectively.

ORCID iDs

Anshu Gupta https://orcid.org/0000-0002-8984-3666
Jonathan Cohn https://orcid.org/0000-0003-1420-6037
Leo Y. Alcorn https://orcid.org/0000-0002-2250-8687
Tiantian Yuan https://orcid.org/0000-0002-9211-3277
Anishya Harshan https://orcid.org/0000-0001-9414-6382
Ben Forrest https://orcid.org/0000-0001-6003-0541
Lisa J. Kewley https://orcid.org/0000-0001-8152-3943
Karl Glazebrook https://orcid.org/0000-0002-3254-9044
Caroline M. Straatman https://orcid.org/0000-0001-5937-4590
Themiya Nanayakkara https://orcid.org/0000-0003-2804-0648
Ivo Labbé https://orcid.org/0000-0002-2057-5376
Casey Papovich https://orcid.org/0000-0001-7503-8482
Michael Cowley https://orcid.org/0000-0002-4653-8637

References

Alcorn, L. Y., Tran, K.-V. H., Kacprzak, G. G., et al. 2016, ApJL, 825, L2
Allen, R. J., Kacprzak, G. G., Glazebrook, K., et al. 2016, ApJL, 834, L11
Barro, G., Faber, S. M., Pérez-González, P. G., et al. 2013, ApJ, 765, 104
Barro, G., Trump, J. R., Koo, D. C., et al. 2014, ApJ, 795, 145
Beck, A. M., Murante, G., Arth, A., et al. 2016, MNRAS, 455, 2110
Bernardi, M., Meert, A., Sheth, R. K., et al. 2017, MNRAS, 467, 2217
Brammer, G. B., Van Dokkum, P. G., Franx, M., et al. 2012, ApJS, 200, 13
Byler, N., Dalcanton, J. J., Conroy, C., & Johnson, B. D. 2017, ApJ, 840, 44
Calzetti, D., Kinney, A. L., & Storchi-Bergmann, T. 1994, ApJ, 429, 582
Cappellari, M., Bacon, R., Bureau, M., et al. 2006, MNRAS, 366, 1126
Chabrier, G. 2003, PASP, 115, 763
Choi, J., Dotter, A., Conroy, C., et al. 2016, ApJ, 823, 102
Cohn, J. H., Leja, J., Tran, K.-V. H., et al. 2018, ApJ, 869, 141
Conroy, C., & Gunn, J. E. 2010, ApJ, 712, 833
Conroy, C., Gunn, J. E., & White, M. 2009, ApJ, 699, 486
Courteau, S., Cappellari, M., de Jong, R. S., et al. 2014, RvMP, 86, 47
Cowley, M. J., Spitler, L. R., Tran, K.-V. H., et al. 2016, MNRAS, 457, 629
Davidzon, I., Ilbert, O., Laigle, C., et al. 2017, A&A, 605, A70
Davies, R. L., Schreiber, N. M. F., Übler, H., et al. 2019, ApJ, 873, 122
Dotter, A. 2016, ApJS, 222, 8
Eggen, O. J., Lynden-Bell, D., & Sandage, A. R. 1962, ApJ, 136, 748
Epinat, B., Tasca, L., Amram, P., et al. 2012, A&A, 539, A92
Fall, S. M., & Efstathiou, G. 1980, MNRAS, 193, 189
Forrest, B., Tran, K.-v. H., Broussard, A., et al. 2018, ApJ, 863, 131
Förster Schreiber, N. M., Genzel, R., Bouché, N., et al. 2009, ApJ, 706, 1364
Genel, S., Dekel, A., & Cacciato, M. 2012, MNRAS, 425, 788
Genel, S., Nelson, D., Pillepich, A., et al. 2018, MNRAS, 474, 3976
Genzel, R., Schreiber, N. M. F., Übler, H., et al. 2017, Natur, 543, 397
Girard, M., Dessauges-Zavadsky, M., Schaerer, D., et al. 2018, A&A, 613, A72
Glazebrook, K. 2013, PASA, 30, 1
Glazebrook, K., Schreiber, C., Labbé, I., et al. 2017, Natur, 544, 71

Gnerucci, A., Marconi, A., Cresci, G., et al. 2011, A&A, 528, A88
Grogin, N. A., Kocevski, D. D., Faber, S. M., et al. 2011, ApJS, 197, 35
Hilz, M., Naab, T., & Ostriker, J. P. 2013, MNRAS, 429, 2924
Hinshaw, G., Larson, D., Komatsu, E., et al. 2013, ApJS, 208, 19
Hung, C. L., Rich, J. A., Yuan, T., et al. 2015, ApJ, 803, 62
Koekemoer, A. M., Faber, S. M., Ferguson, H. C., et al. 2011, ApJS, 197, 36
Kriek, M., van Dokkum, P. G., Labbé, I., et al. 2009, ApJ, 700, 221
Krumholz, M. R., & Burkhart, B. 2016, MNRAS, 458, 1671
Krumholz, M. R., Burkhart, B., Forbes, J. C., & Crocker, R. M. 2018,
    MNRAS, 477, 2716
Lang, P., Schreiber, N. M., Genzel, R., et al. 2017, in IAU Symp. 321,
    Formation and Evolution of Galaxy Outskirts (Cambridge: Cambridge
    Univ. Press), 315
Law, D. R., Steidel, C. C., Chen, Y., et al. 2018, ApJ, 866, 119
Law, D. R., Steidel, C. C., Erb, D. K., et al. 2009, ApJ, 697, 2057
Lee, J., & Yi, S. K. 2013, ApJ, 766, 38
Leja, J., Carnall, A. C., Johnson, B. D., Conroy, C., & Speagle, J. S. 2019a,
    ApJ, 876, 3
Leja, J., Johnson, B. D., Conroy, C., et al. 2019b, ApJ, 877, 140
Leja, J., Johnson, B. D., Conroy, C., van Dokkum, P. G., & Byler, N. 2017,
    ApJ, 837, 170
Livermore, R. C., Jones, T. a., Richard, J., et al. 2015, MNRAS, 450, 1812
Madau, P., & Dickinson, M. 2014, ARA&A, 52, 415
Mandelker, N., Dekel, A., Ceverino, D., et al. 2014, MNRAS, 443, 3675
Marinacci, F., Vogelsberger, M., Pakmor, R., et al. 2018, MNRAS, 480, 5113
Martin, D. C., O'Sullivan, D., Matuszweski, M., et al. 2019, NatAs, 3, 822
Maseda, M. V., van der Wel, A., da Cunha, E., et al. 2013, ApJL, 778, L22
Maseda, M. V., van der Wel, A., Rix, H.-w., et al. 2014, ApJ, 791, 17
McLean, I. S., Steidel, C. C., Epps, H. W., et al. 2012, Proc. SPIE, 8446,
    84460J
Naiman, J. P., Pillepich, A., Springel, V., et al. 2018, MNRAS, 477, 1206
Nanayakkara, T., Glazebrook, K., Kacprzak, G. G., et al. 2016, ApJ, 828, 1
Nelson, D., Pillepich, A., Springel, V., et al. 2018, MNRAS, 475, 624
Nelson, E., Van Dokkum, P., Franx, M., et al. 2014, Natur, 513, 394
Newman, S. F., Buschkamp, P., Genzel, R., et al. 2013, ApJ, 781, 21
Newville, M., Stensitzki, T., Allen, D. B., et al. 2016, Lmfit: Non-Linear Least-
    Square Minimization and Curve-Fitting for Python, v0.9.8., Astrophysics
    Source Code Library, ascl:1606.014

Nipoti, C., Treu, T., Auger, M. W., & Bolton, A. S. 2009, ApJ, 706, 86
Paxton, B., Bildsten, L., Dotter, A., et al. 2011, ApJS, 192, 3
Paxton, B., Cantiello, M., Arras, P., et al. 2013, ApJS, 208, 4
Paxton, B., Marchant, P., Schwab, J., et al. 2015, ApJS, 220, 15
Pedregosa, F., Varoquaux, G., Gramfort, A., et al. 2012, 12, 2825
Peng, C. Y., Ho, L. C., Impey, C. D., & Rix, H. W. 2010, ApJ, 139, 2097
Pillepich, A., Nelson, D., Hernquist, L., et al. 2018, MNRAS, 475, 648
Price, S. H., Kriek, M., Barro, G., et al. 2019, arXiv:1902.09554
Price, S. H., Kriek, M., Shapley, A. E., et al. 2015, ApJ, 819, 80
Rodriguez-Gomez, V., Genel, S., Vogelsberger, M., et al. 2015, MNRAS,
    449, 49
Rodriguez-Gomez, V., Pillepich, A., Sales, L. V., et al. 2016, MNRAS,
    458, 2371
Saintonge, A., Lutz, D., Genzel, R., et al. 2013, ApJ, 778, 2
Searle, L., & Zinn, R. 1978, ApJ, 225, 357
Simons, R. C., Kassin, S. A., Trump, J. R., et al. 2016, ApJ, 830, 14
Sobral, D., Swinbank, A. M., Stott, J. P., et al. 2013, ApJ, 779, 139
Springel, V., Pakmor, R., Pillepich, A., et al. 2018, MNRAS, 475, 676
Stott, J. P., Swinbank, A. M., Johnson, H. L., et al. 2016, MNRAS, 457,
    1888
Straatman, C. M. S., Glazebrook, K., Kacprzak, G. G., et al. 2017, ApJ, 839, 57
Straatman, C. M. S., Spitler, L. R., Quadri, R. F., et al. 2016, ApJ, 830, 1
Suzuki, T. L., Kodama, T., Onodera, M., et al. 2017, ApJ, 849, 39
Tacconi, L. J., Genzel, R., Saintonge, A., et al. 2018, ApJ, 853, 179
Teklu, A. F., Remus, R.-s., Dolag, K., et al. 2018, ApJL, 854, L28
Tiley, A. L., Swinbank, A. M., Harrison, C. M., et al. 2019, MNRAS, 485, 934
Tran, K. V. H., Forrest, B., & Alcorn, L. Y. 2020, ApJ, submitted
Tran, K.-V. H., Nanayakkara, T., Yuan, T., et al. 2015, ApJ, 811, 28
Turner, O. J., Cirasuolo, M., Harrison, C. M., et al. 2017, MNRAS, 471, 1280
Übler, H., Förster Schreiber, N. M., Genzel, R., et al. 2017, ApJ, 842, 121
Übler, H., Genzel, R., Wisnioski, E., et al. 2019, ApJ, 880, 48
van de Sande, J., Kriek, M., Franx, M., et al. 2013, ApJ, 771, 85
van der Wel, a., Franx, M., van Dokkum, P. G., et al. 2014, ApJ, 788, 28
Wellons, S., Torrey, P., Ma, C. P., et al. 2016, MNRAS, 456, 1030
White, S. D. M., & Rees, M. J. 1978, MNRAS, 183, 341
Wiseman, P., Perley, D. A., Schady, P., et al. 2017, A&A, 607, A107
Wisnioski, E., Förster Schreiber, N. M., Wuyts, S., et al. 2015, ApJ, 799, 209
Zabl, J., Bouché, N. F., Schroetter, I., et al. 2019, MNRAS, 485, 1961